






# High-speed silicon modulators for the 2 $\mu\text{m}$ wavelength band

WEI CAO,<sup>1</sup>  DAVID HAGAN,<sup>3</sup> DAVID J. THOMSON,<sup>1</sup> MILOŠ NEDELJKOVIĆ,<sup>1</sup>  CALLUM G. LITTLEJOHNS,<sup>1,2</sup> ANDY KNIGHTS,<sup>3</sup> SHAI-UL ALAM,<sup>1</sup> JUNJIA WANG,<sup>1,4</sup> FREDERIC GARDES,<sup>1</sup>  WEIWEI ZHANG,<sup>1</sup> SHENGHAO LIU,<sup>1</sup> KE LI,<sup>1</sup> MOHAMED SAID ROUFED,<sup>2</sup> GUO XIN,<sup>2</sup> WANJUN WANG,<sup>2</sup> HONG WANG,<sup>2</sup> GRAHAM T. REED,<sup>1</sup> AND GORAN Z. MASHANOVICH<sup>1,5,\*</sup>

<sup>1</sup>Optoelectronics Research Centre, University of Southampton, University Road, Southampton, Hampshire SO17 1BJ, UK

<sup>2</sup>Silicon Technologies Centre of Excellence, Nanyang Technological University, Singapore 639798, Singapore

<sup>3</sup>Department of Engineering Physics, McMaster University, Hamilton, Ontario L8S 4L7, Canada

<sup>4</sup>Cambridge Graphene Centre, Engineering Department, University of Cambridge, Cambridge CB3 0FA, UK

<sup>5</sup>School of Electrical Engineering, University of Belgrade, 11120 Belgrade, Serbia

\*Corresponding author: g.mashanovich@soton.ac.uk

Received 30 March 2018; revised 30 June 2018; accepted 2 July 2018 (Doc. ID 327168); published 28 August 2018

The 2  $\mu\text{m}$  wavelength band has become a promising candidate to be the next communication window. We demonstrate high-speed modulators based on a 220 nm silicon-on-insulator platform working at a wavelength of 1950 nm, using the free carrier plasma dispersion effect in silicon. A Mach–Zehnder interferometer modulator and a microring modulator have been characterized. At 1950 nm, the carrier-depletion modulator operates at a data rate of 20 Gbit/s with an extinction ratio of 5.8 dB and insertion loss of 13 dB. The modulation efficiency ( $V_{\pi} \cdot L_{\pi}$ ) is 2.68 V·cm at 4 V reverse bias. The device operation is broadband, and we also characterize its performance at 1550 nm. At 1550 nm, an open eye is obtained at 30 Gbit/s. The difference in bandwidth is caused by the bandwidth limit of the 2  $\mu\text{m}$  measurement setup. We also show a ring modulator paired with a low power integrated driver working in hybrid carrier depletion and injection mode at a data rate of 3 Gbit/s with power consumption of 2.38 pJ/bit in the 2  $\mu\text{m}$  wavelength range. This work is a proof of principle demonstration and paves a route toward a full silicon-based transceiver in the 2  $\mu\text{m}$  window.

Published by The Optical Society under the terms of the [Creative Commons Attribution 4.0 License](https://creativecommons.org/licenses/by/4.0/). Further distribution of this work must maintain attribution to the author(s) and the published article's title, journal citation, and DOI.

**OCIS codes:** (130.4110) Modulators; (060.4080) Modulation; (060.4510) Optical communications; (130.0130) Integrated optics; (130.3120) Integrated optics devices; (250.0250) Optoelectronics.

<https://doi.org/10.1364/OPTICA.5.001055>

## 1. INTRODUCTION

Fiber-based telecommunication systems have sustained a startling increase in capacity demand since the inception of the internet. New technologies such as erbium-doped fiber amplifiers (EDFAs), wave division multiplexing (WDM), and high-spectral efficiency coding have allowed bandwidth capacity to keep up with demand [1]. However, with the latest digital-signal-processing (DSP)-assisted coherent detection, we are approaching the theoretical capacity limit of conventional single mode fibers (SMFs) [2]. If this trend proceeds, a “capacity crunch” may happen in the future, where the current communication system can no longer sustain the bandwidth demands of the internet [1]. The crisis might not be imminent as it can be addressed by funding more infrastructure with multiple parallel links and by trimming down the transmitted data itself via compression. But neither solution can be scaled up indefinitely as multiple links and data compression imply substantial energy consumption. The more elegant solution is to

develop new technologies that enable the next round of capacity boost.

One promising option is the use of low-loss hollow-core photonic bandgap fibers (HC-PBGFs). The optical mode resides largely in the air core of HC-PBGFs, hence minimizing the Rayleigh scattering ( $\lambda^{-4}$  wavelength dependence), which is the dominant source of loss in standard SMFs. By considering remaining loss mechanisms, namely surface scattering ( $\lambda^{-3}$  wavelength dependence) and infrared absorption loss of the silicon dioxide, the predicted lowest-loss windows are shifted from 1550 nm to the 1900–2100 nm band and the theoretical minimum loss achievable is below 0.1 dB/km [3,4]; this loss is lower than the best conventional SMF (0.1484 dB/km) [5]. Furthermore, the nonlinearity of HC-PBGF can be highly reduced as well as engineered to a large extent, owing to the fact that only a fraction of the light propagates through the silica [6]. With the aforementioned low loss and low nonlinearity, and some

other advantages including low latency [7], low thermal sensitivity [8], and high radiation hardness [9], HC-PBGF shows great potential as a candidate building block of future telecommunication system.

The proposed HC-PBGF based communication system [10] should operate at around 2  $\mu\text{m}$  to take advantage of the low-loss window of the fiber. Coincidentally, the optical gain window of thulium-doped fiber amplifiers (TDFAs) resides at around 1910–2020 nm, and it can be used as the equivalent to EDFAs in a 2  $\mu\text{m}$  system [11,12]. Another advantage of such a system is the compatibility with silicon photonics, as the material loss of silicon dioxide is low at 2  $\mu\text{m}$ , and low propagation loss strip and rib waveguides on an silicon-on-insulator (SOI) platform have been demonstrated [13]. This allows for potentially fully integrated high-performance transceivers mass produced with reduced cost by leveraging complementary metal-oxide-semiconductor (CMOS)-compatible fabrication processes. Recent breakthroughs in hollow-core photonic bandgap fibers drive the 2  $\mu\text{m}$  system from a mere proposal toward applications. Researchers have demonstrated a 3.8 km long hollow-core fiber with loss as low as 3 dB/km at 2  $\mu\text{m}$  [14,15]. Several silicon-photonics-based bulk defect-mediated absorption (BDA) types of detector in 2  $\mu\text{m}$  have been successfully demonstrated. Ackert *et al.* [16] have realized the highest data rate defect photodiode (PD), which can operate at 20 Gbit/s at 2  $\mu\text{m}$  in silicon.

However, to date there have been few demonstrations of high-speed 2  $\mu\text{m}$  group-IV-material-based modulators. In the near-infrared (NIR), plasma-dispersion-effect-based modulators show convincing performance, as well as CMOS compatibility [17], with data rates of up to 90 Gbit/s [18]. A theoretical analysis of the plasma dispersion effect in the midinfrared (MIR) has been performed [19], and suggests that the effect is present in the 2  $\mu\text{m}$  regime and is even moderately stronger than in the NIR. However, to our knowledge, the only demonstration of a 2  $\mu\text{m}$  wavelength high-speed modulator using silicon carrier effect was made by IBM, which has reported SOI carrier injection modulators operating at 2165 nm. Using a pre-emphasis drive signal, the device reached a bitrate of 3 Gbit/s [20]. There have been several high-speed transmission demonstrations over HC-PBGF in 2  $\mu\text{m}$ , in which the transceivers resort to directly modulated lasers or a commercially available discrete LiNbO<sub>3</sub> Mach-Zehnder interferometer modulator (MZM) (e.g., MX2000-LN-10, Photline) [14,21]. The latest results show an eight-channel system with a total capacity of 100 Gbit/s at 2  $\mu\text{m}$ . The system consists of a mixture of four internal modulation channels and four external modulation channels. The direct modulated laser is based on a In<sub>0.75</sub>Ga<sub>0.25</sub>As quantum well and with a bandwidth of 5.1 GHz. The LiNbO<sub>3</sub> MZM-based external modulation requires relatively large 9.5 V switching voltage [21], which is impractical to integrate. A four-channel system is also shown with 10 Gb/s data rate per channel, where the newly developed 2  $\mu\text{m}$  InP MZM replaces the LiNbO<sub>3</sub> counterpart [22]. Although the InP MZM is significantly more compact than LiNbO<sub>3</sub> devices, it still lacks CMOS compatibility. Theoretical proof of concept analysis of modulation using aluminium nitride [23] and GeSn quantum wells [24] has also been published. On the germanium-on-silicon platform, an all-optical modulator based on free-carrier absorption has been demonstrated working at around 55 MHz across the 2–3.2  $\mu\text{m}$  wavelength range [25]. Toward longer wavelengths, an electroabsorption modulator is shown operating at 3.8  $\mu\text{m}$  with

a data rate of at least 6 MHz [26]. Optical attenuators (VOAs) based on free-carrier injection have also been demonstrated on both SOI [27] and germanium-on-insulator platforms [28].

In this paper we demonstrate the state of the art silicon-photonics-based high-speed modulators and is organized as follows. The equation of the free-carrier effect in silicon at 2  $\mu\text{m}$  is first given, followed by a brief description of the methodology of the simulation. Then the simulation results and design choices are presented. Next, the high-speed 2  $\mu\text{m}$  characterization setup used to test the devices in this paper is described. Finally, DC and high-speed modulation performance for both a Mach-Zehnder interferometer (MZI) modulator and a ring modulator are presented with analysis.

## 2. SIMULATION AND DESIGN

In 1987 Soref and Bennett [29] published semi-empirical predictions for the changes in absorption coefficient and refractive index due to changes in the electron and hole concentrations in silicon at 1300 nm and 1550 nm wavelengths that guided designs of generations of free-carrier modulators at these wavelengths. Nedeljkovic *et al.* [19] more recently used the same method to expand on Soref and Bennett's work [29], extending the wavelength range of the equations from 1.3–1.55  $\mu\text{m}$  to 1.3–14  $\mu\text{m}$ . The free-carrier-effect predictions for 2  $\mu\text{m}$  are given in Eqs. (1) and (2):

$$\begin{aligned} -\Delta n(2 \mu\text{m}) &= \Delta n_e(2 \mu\text{m}) + \Delta n_h(2 \mu\text{m}) \\ &= 1.91 \times 10^{-21} \times \Delta N_e^{0.992} + 2.28 \times 10^{-18} \times \Delta N_h^{0.841}, \end{aligned} \quad (1)$$

$$\begin{aligned} \Delta \alpha(2 \mu\text{m}) &= \Delta \alpha_e(2 \mu\text{m}) + \Delta \alpha_h(2 \mu\text{m}) \\ &= 3.22 \times 10^{-20} \times \Delta N_e^{1.149} + 6.21 \times 10^{-20} \times \Delta N_h^{1.119}, \end{aligned} \quad (2)$$

where  $n$  is the real part of the refractive index and  $\alpha$  is the absorption coefficient ( $\text{cm}^{-1}$ ) defined by  $\alpha = 4\pi k/\lambda$ , where  $k$  is the imaginary part of refractive index and  $\lambda$  is the wavelength (2  $\mu\text{m}$  in this case);  $\Delta n_e$  is the refractive index change due to electrons;  $\Delta n_h$  is the refractive index change due to holes;  $\Delta \alpha_e$  is the absorption coefficient change due to electrons;  $\Delta \alpha_h$  is the absorption coefficient change due to holes;  $N_e$  is the electron concentration ( $\text{cm}^{-3}$ ); and  $N_h$  is the hole concentration ( $\text{cm}^{-3}$ ).

According to these equations silicon exhibits a stronger free-carrier effect at 2  $\mu\text{m}$  than at both 1300 nm and 1500 nm; i.e., there is a larger change of both the real part of the refractive index and of the absorption coefficient when the electron and hole concentrations are changed. An experimental demonstration of a broadband carrier-injection-based VOA indeed shows a trend of increasing attenuation from 1300 nm toward 2500 nm [27].

The refractive index change causes a phase shift of the light propagating through the phase shifter. Phase modulation can be converted into amplitude modulation by integrating such a phase shifter into a MZI or microring resonator.

The phase shifter response is analyzed by a combination of electrical device simulation using Silvaco TCAD tools and optical device simulation using a Matlab-based waveguide mode solver [30]. The Silvaco simulation software was used to build the electrical device model. The electrical device model was used to simulate the free-carrier distribution throughout the phase shifter

cross-section with (a) different reverse bias/forward bias voltages for obtaining the DC response and with (b) a step rise and a step fall in bias voltage for analyzing the transient response to extract the radio frequency (RF) performance. In Matlab, the free-carrier distribution is translated into a change in complex refractive index, where Eqs. (1) and (2) [19] are used. A Matlab-based optical mode solver then finds the mode in the waveguide considering both the calculated perturbation in refractive index due to the free-carrier effect and the baseline material refractive index. Finally, the performance of the device is evaluated through the effective refractive index and loss of each optical mode.

### A. MZI Modulator Design

Figure 1 shows a schematic of the cross-section of the phase shifter in the MZI modulators and ring modulators. Both types of modulator share a similar cross-section design, but the dimensions are different. The MZI modulators exploit the carrier depletion effect. Devices are fabricated on 220 nm SOI wafers with a 2  $\mu\text{m}$  buried oxide (BOX) layer, in order to maintain compatibility with standard silicon thicknesses used in NIR silicon photonics multiproject wafer foundry services. The silicon rib waveguide is 550 nm wide ( $W_{\text{WG}}$ ) and etched by 90 nm in the slab region ( $h_{\text{WG}}$ ).

According to the optical mode simulations in Fig. 2(c), at 1950 nm, the rib waveguide is single mode for widths up to

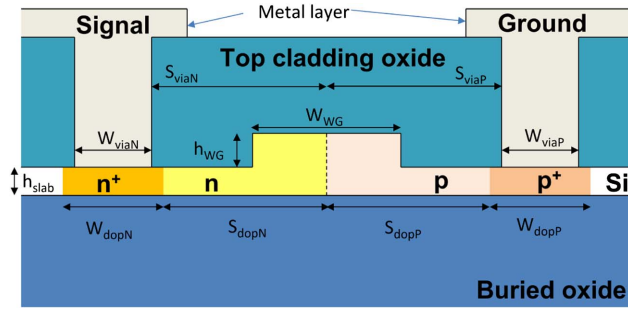


Fig. 1. Cross-section of the phase shifter for MZI and ring modulator.

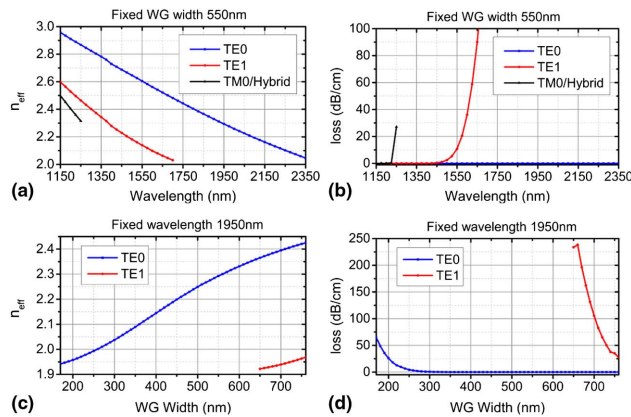


Fig. 2. Mode analysis of a rib waveguide in the 220 nm SOI platform with 90 nm slab thickness. The calculated loss does not consider roughness. (a) Simulated optical mode effective refractive index with fixed waveguide width of 550 nm. (b) Simulated optical mode loss with fixed waveguide width of 550 nm. (c) Simulated optical mode effective refractive index with fixed wavelength of 1950 nm. (d) Simulated optical mode loss with fixed wavelength of 1950 nm.

650 nm. However, as the waveguide width gets narrower, the mode becomes less confined, and this can reduce the efficiency of a modulator. A 600 nm waveguide width is a preferable choice at 2  $\mu\text{m}$ , and it is used in our ring modulator design; at 1550 nm, the waveguide becomes too multimode, and since we target operation at both 1550 nm and at 2  $\mu\text{m}$  on our MZI modulator, a narrower 550 nm width is adopted. The single mode cutoff wavelength for a 550 nm wide waveguide is 1700 nm as shown in Fig. 2(a). At 1550 nm, Fig. 2(b) shows that the loss of the TE1 mode is about 10 dB/cm higher than the TE0 mode. Such a waveguide is still usable in the C-band in our “single mode” modulator optimization.

The PN junction position is in the center of the waveguide, and the highly doped regions are 1.125  $\mu\text{m}$  ( $S_{\text{dop}N}$ ) and 1.025  $\mu\text{m}$  ( $S_{\text{dop}P}$ ) away from the junction. The target doping concentrations in the simulation are  $3 \times 10^{17} \text{ cm}^{-3}$ ,  $8.5 \times 10^{17} \text{ cm}^{-3}$ ,  $1 \times 10^{20} \text{ cm}^{-3}$ , and  $1 \times 10^{20} \text{ cm}^{-3}$  for  $n$ ,  $p$ ,  $n^+$ , and  $p^+$ , respectively.

The simulated free-carrier concentration against various reverse biases' voltage is illustrated in Fig. 3. The depletion region width enlarges with increasing reverse bias voltages. This effect is independent of optical wavelength.

Figure 4 shows how such a phase shifter design responds to 4 V reverse bias when the wavelength is varied. The dashed line in the graph represents the loss derived from a similar device but with

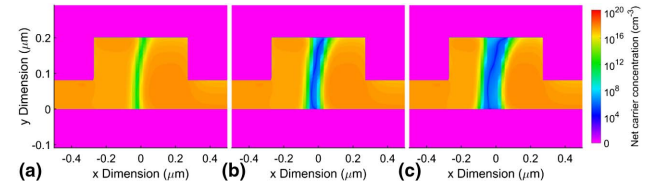


Fig. 3. Simulated net carrier concentration of the phase shifter under various reverse biases. (a) Reverse bias 0 V. (b) Reverse bias 2 V. (c) Reverse bias 4 V.

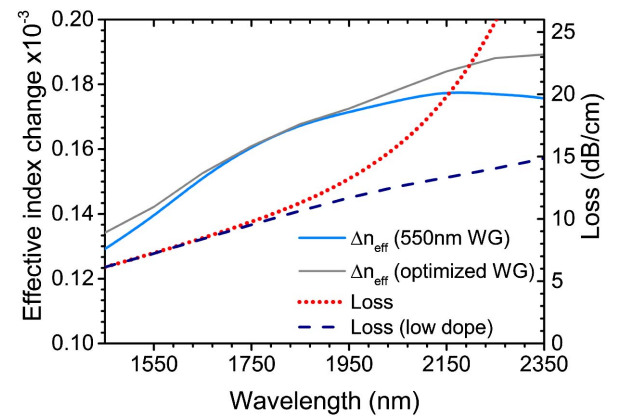


Fig. 4. Simulated effective refractive index change and loss of a phase shifter with the adopted design due to carrier effect under 4 V reverse bias across the 1450–2250 nm wavelength range. The blue line shows the refractive index change for the 550 nm wide waveguide. The light gray line shows the refractive index change for a waveguide width optimized at each wavelength, with a width ranging from 450–650 nm. The red-dotted line shows loss with the adopted 550 nm wide waveguide. The dark blue-dashed line is the simulated loss from a similar phase shifter design but with larger 1.7  $\mu\text{m}$   $S_{\text{dop}P}$  and  $S_{\text{dop}N}$  to serve as the reference loss of the low-doped region.



doping separations  $S_{\text{dop}P}$  and  $S_{\text{dop}N}$  increased to  $1.7 \mu\text{m}$  to almost eliminate the loss contribution due to mode overlap with the highly doped region. We notice that the change in refractive index rises as the wavelength increases from  $1500 \text{ nm}$  toward  $2000 \text{ nm}$ . The overall loss shown in the dotted curve also increases, and even without the absorption from the highly doped regions, loss still follows a rising trend. This is in accordance with the trend predicted by the generalized equation of the carrier effect [19]; i.e., both changes in refractive index and loss due to carrier effect are higher at  $2 \mu\text{m}$  than at  $1.55 \mu\text{m}$ . However, if fixing the waveguide width at  $550 \text{ nm}$ , as depicted by the blue curve, there is a level off in the rise of change in refractive index after  $2000 \text{ nm}$ , and there is even a slight drop beyond  $2150 \text{ nm}$ . The reason is that the mode profile size is significantly larger at longer wavelengths, and the effective overlap between the optical mode and the carrier changing region is diluted. Although the carrier effect is higher at longer wavelengths, the overall effect is the result of both. The light gray curve shows the effective index change for an optimized waveguide width at each wavelength. The general trend is that increasing the waveguide width increases the effective index change at longer wavelengths. As we can see, the  $550 \text{ nm}$  width strikes a good balance between the  $1550 \text{ nm}$  and  $2 \mu\text{m}$  wavelengths.

During the design process, two important dimension parameters have been swept to analyze their effects. The first is the separation between the high doping sections and the optical waveguide core. To form Ohmic contacts, a high doping concentration (e.g.,  $1 \times 10^{20} \text{ cm}^{-3}$ ) at the interface of silicon and metal is required. According to Fig. 5(a), when varying the doping separation, there is a trade-off between device bandwidth and free-carrier loss. The device bandwidth rises as the high doping separation decreases, due to reduced access resistance. However, when the high doping is too close to the waveguide core, the overlap between the optical mode and free carriers in the high doping region increases, resulting in significant optical loss. Therefore, a trade-off between device bandwidth and device loss should be considered. We note that at  $1950 \text{ nm}$  the optical mode size in

the waveguide must be larger than at  $1550 \text{ nm}$ ; therefore a larger separating  $S_{\text{dop}P} + S_{\text{dop}N}$  is required, theoretically reducing the bandwidth of the device. In our design, we chose  $S_{\text{dop}P}$  of  $1.025 \mu\text{m}$  for  $p+$  doping and  $S_{\text{dop}N}$  of  $1.125 \mu\text{m}$  for  $n+$  doping. The reason for the asymmetrical separation is that  $p$ -type silicon absorbs less optical power than  $n$ -type silicon for the same doping concentration, so it can be positioned closer to the waveguide core to enhance RF performance; while  $n$ -type silicon has higher loss, it also has greater conductivity, so we can afford for it to be placed farther away to reduce the overall loss. In this case, the simulated loss is below  $20 \text{ dB/cm}$  (at reverse bias of  $4 \text{ V}$ ), and the device bandwidth is above  $75 \text{ GHz}$ . Figure 5(b) shows that the doping separation has very little effect on the efficiency of the modulator, as the parameters of the low doping concentration region have a more direct impact on the PN junction geometry and position, and hence on the device efficiency. The PN junction position is the second major parameter. By scanning its position, as illustrated in Figs. 5(c) and 5(d), we see that with the selected doping concentrations the device has the lowest loss and highest efficiency when it is placed near the center of the waveguide, because the maximum overlap of the optical mode and depletion region is achieved. The bandwidth, however, increases when the junction position is close to the edge of the waveguide core, because in this case the PN junction is partially in the slab region of the waveguide and has a reduced cross-section compared to in the core region. This results in lower capacitance and hence higher bandwidth. However, achieving this condition comes at the cost of significantly higher loss and lower efficiency. If the doping separation is chosen properly, the simulated bandwidth should be greater than  $75 \text{ GHz}$  regardless of junction position. In our design, we choose a  $0 \text{ nm}$  junction offset.

In the  $2 \mu\text{m}$  band the optical mode profile is inherently larger than in the C-band. The highly doped regions and metal contact vias should therefore be positioned farther away, resulting in inferior RF performance. This could, however, be mitigated by migrating to a thicker SOI platform with, for example,  $340 \text{ nm}$  or  $500 \text{ nm}$  silicon top layer. In these cases, given similar slab thickness as in the  $220 \text{ nm}$  SOI platform (to maintain similar RF properties), the optical mode retreats further from the slab region and is better confined in the rib part of the waveguide, hence minimizing the interaction with the highly doped regions in the slab.

Figure 6 is an optical microscope image of the core of the MZI modulator. The device is fabricated by IME in a multiproject wafer (MPW) run with customized doping concentration. The phase shifter is incorporated into both arms of a MZI, to convert the phase shift into an amplitude shift. An arm length difference of  $180 \mu\text{m}$  is used in the MZI to obtain a sinusoidal response and to facilitate the characterization. The device is designed with Y-splitters instead of multimode interferometers (MMIs) in the MZI, and it uses butt coupling, so the modulator operating wavelength range is not limited by the relatively narrow bandwidth of MMIs or grating couplers. The spectral bandwidth of the phase

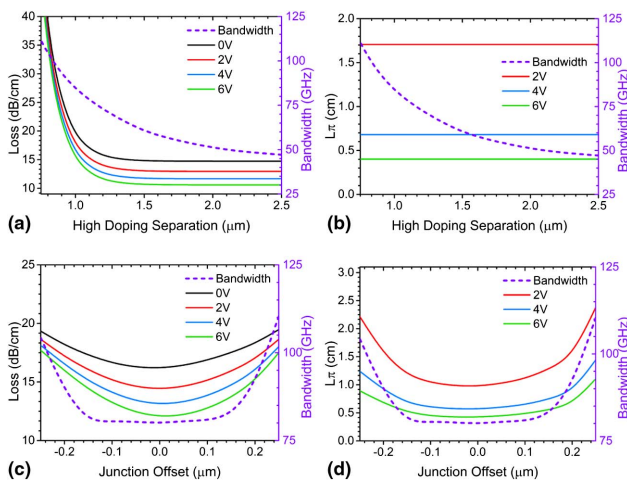


**Fig. 5.** MZI modulator phase shifter simulation in  $1950 \text{ nm}$ . (a) Simulated loss versus high concentration doping separation with fixed junction offset 0. (b) Simulated  $L_\pi$  versus high concentration doping separation with fixed junction offset 0. (c) Simulated loss versus junction offset with fixed high concentration doping separation ( $S_{\text{dop}N}$ )  $1.125 \mu\text{m}$  for  $n+$  and ( $S_{\text{dop}P}$ )  $1.025 \mu\text{m}$  for  $p+$ . (d) Simulated  $L_\pi$  versus high concentration doping separation with fixed junction offset 0.

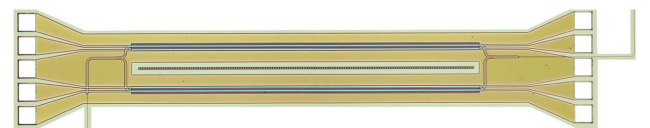


**Fig. 6.** Optical microscope image of the MZI modulator.

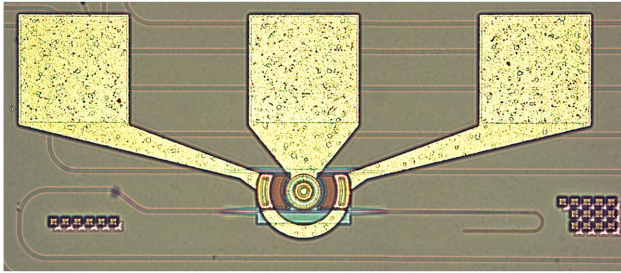


Fig. 7. Optical microscope image of the ring modulator.

shifter itself is only limited by the single mode waveguide bandwidth. A traveling wave electrode design is used with GSGSG pads on both ends and a tapered down section along the phase shifter.

### B. Ring Modulator Design

Figure 7 shows an optical microscope image of the designed ring modulator. The device is fabricated by IME in an MPW run with default IME doping concentration. Devices are fabricated on 220 nm SOI wafers with a 2  $\mu\text{m}$  BOX layer, similar to the MZI modulators. The silicon rib waveguide is 600 nm wide ( $W_{\text{WG}}$ ) and etched by 90 nm in the slab region ( $h_{\text{WG}}$ ). The PN junction position is again centred in the waveguide and the highly doped regions are 1.3  $\mu\text{m}$  ( $S_{\text{dop},N}$  and  $S_{\text{dop},P}$ ) away from the junction. The target doping concentrations in the simulation are  $1.5 \times 10^{17} \text{ cm}^{-3}$ ,  $3.5 \times 10^{17} \text{ cm}^{-3}$ ,  $1 \times 10^{20} \text{ cm}^{-3}$ , and  $1 \times 10^{20} \text{ cm}^{-3}$  for  $n$ ,  $p$ ,  $n+$ , and  $p+$ , respectively. The electrically active region covers 64% of the ring with 10  $\mu\text{m}$  radius. While the separation of the highly doped regions can influence the electrical bandwidth of both MZI and ring modulators, the latter can be bandwidth-limited by the photon lifetime of the ring. Tuning the separation of these doped regions results in a trade-off between modulation bandwidth and optical modulation amplitude. One may passively decrease the photon lifetime by means of a small radius ring, which will incur additional optical bending loss; also, an add-drop ring design may be used that naturally has additional coupling loss at the second bus waveguide. Electrodes are used with a GSG pad configuration.

### 3. EXPERIMENTAL SETUP

Expanding the measurement capability to 2  $\mu\text{m}$  requires new components along the optical path, as most 1300/1550 nm equipment is incompatible with the 2  $\mu\text{m}$  wavelength. Some bespoke 2  $\mu\text{m}$  equipment has been used: an EOT ET-5000 high-speed 2  $\mu\text{m}$  InGaAs detector, with a rated bandwidth of >12.5 GHz and peak responsivity of 1.3 A/W at 2000 nm; an amplified Thorlabs low speed 2  $\mu\text{m}$  InGaAs detector, with peak responsivity of 1.3 A/W at 2300 nm and maximum internal gain of 70 dB; Thorlabs SM2000 silica fibers with 11  $\mu\text{m}$  core diameter and optimized for 2  $\mu\text{m}$ ; and a Thorlabs TLK-L1950R tunable laser, which is tunable from 1890–2020 nm. We have also used a thulium-doped fiber amplifier (TDFA) to increase the optical power, similar to the one presented in Ref. [12]. It uses an EDFA as a pump source, and gives 13 dB gain. Since the TDFA is polarization sensitive, a polarization controller before the signal input is essential. As the peak output power of the tunable laser is only 7 mW, the TDFA is used before

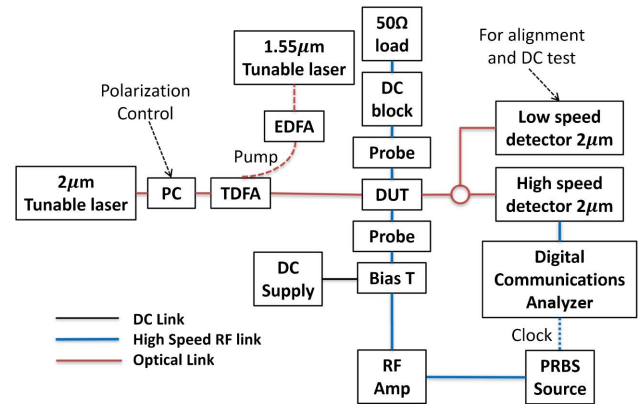


Fig. 8. High-speed RF measurement set up for 2  $\mu\text{m}$  wavelength modulator.

the device under test (DUT). The low-speed but more sensitive detector is used during alignment and DC measurements.

During the high-speed testing (Fig. 8), a pseudorandom binary sequence generator (PRBS) is used to generate a bit sequence. The high-speed electrical signal is then amplified by a three-stage Centellax OA4MVM3 amplifier and applied to the DUT with an RF probe. A bias tee is used to combine DC bias and high-speed RF signal. While testing the MZI with traveling wave electrodes, a second probe and external 50  $\Omega$  termination load and DC block are used. The modulated light is then fed into the high-speed InGaAs detector and then analyzed by the digital communication analyzer (DCA). The DCA model is Keysight Infiniium DCA-X 86100D with Agilent 86116C-040 plugin module.

Compared to the conventional 1300/1550 nm setup, there are limitations in the 2  $\mu\text{m}$  system. The high-speed detector had a nominal bandwidth of >12.5 GHz, limiting the speed at which we could measure the modulator to around 20 Gbit/s and with reduced extinction ratio. A signal faster than 20 Gbit/s cannot operate with the detector.

Moreover, the limited power budget of the 2  $\mu\text{m}$  system often leads to a decent eye being masked by the noise floor of the digital-to-analog converter; hence, an open eye is hard to discern. In the case of RF testing of the 2  $\mu\text{m}$  ring modulator, a linear amplifier (SHF S804A) with 22 dB gain is inserted between the detector and DCA. The signal will degrade to some extent but is amplified enough to obtain a healthy signal-to-noise ratio.

## 4. RESULTS AND ANALYSIS

### A. MZI Modulator under Carrier Depletion

We tested and confirmed that the device transmits and modulates at both 1550 nm and 1950 nm. The modulation efficiency ( $V_{\pi} \cdot L_{\pi}$ ) at a reverse bias of 4 V is  $2.02 \text{ V} \cdot \text{cm}$  at 1550 nm and  $2.68 \text{ V} \cdot \text{cm}$  at 1950 nm. In the experiment, the MZI modulator comprising a 1.5 mm long phase shifter is driven in a singled arm, and the phase shift measured is shown in Fig. 9. It can be seen that the response agrees reasonably well with the simulation predictions for both wavelengths.

The high-speed RF characterization is performed by applying an amplified high-speed  $2^7 - 1$  pseudorandom-bit-stream on-off key signal with a peak-to-peak amplitude of 4 V. A DC bias applied simultaneously to the device. The overall scanning voltage

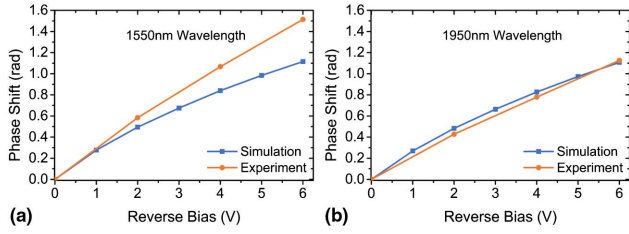


**Fig. 9.** Experimental and simulated phase shift for a MZI modulator with 0.15 cm long phase shifter. (a) Phase shift at 1550 nm. (b) Phase shift at 1950 nm.

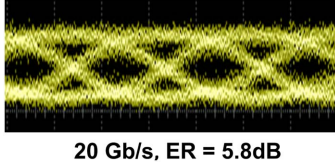


**Fig. 10.** Eye diagram for MZI modulator at data rate of 20 Gb/s at 1950 nm wavelength. Extinction ratio is 5.8 dB.

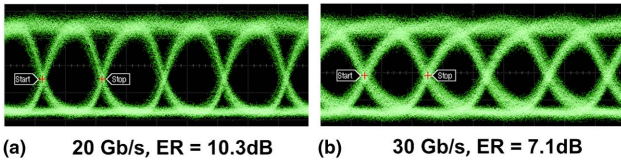


**Fig. 11.** Eye diagram for MZI modulator at 1550 nm wavelength. (a) Data rate is 20 Gb/s, extinction ratio is 10.3 dB. (b) Data rate is 30 Gb/s, extinction ratio is 7.1 dB.

is from  $-4.5$  to  $-0.5$  V. At 1950 nm, an open eye is obtained at 8 Gbit/s with an extinction ratio of 7.6 dB and 20 Gbit/s with extinction ratio of 5.8 dB, as shown in Fig. 10. At 1550 nm, the device modulates at 20 Gbit/s with an extinction ratio of 10.3 dB, as in Fig. 11(a), and 30 Gbit/s with an extinction ratio of 7.1 dB, as in Fig. 11(b).

According to the simulation, the MZI modulator should give similar RF performance for both 1550 nm and 1950 nm wavelengths. The power budget of the system, however, is lower at 1950 nm, rendering the eye diagram at 1950 nm noisier than at 1550 nm. Furthermore, the insertion loss of the device at 1950 nm is measured as 13 dB, which is significantly higher than was measured at 1550 nm (4 dB). The difference is partially due to the stronger plasma dispersion effect and a larger mode overlap with the highly doped region in the 2  $\mu$ m band. According to our simulations these factors contribute to around only 1 dB additional loss for a 1.5 mm long phase shifter. The remaining difference can be attributed to the loss from metal absorption in areas where the waveguide passes directly below the metal layer. The vertical separation between the top of the silicon waveguide and the bottom of the metal layer is only 600 nm, and because the optical mode at 1950 nm is substantially larger, there is greater overlap with the metal. This could be corrected in the next fabrication run either by increasing the silica top cladding thickness to more than 1.0  $\mu$ m, or by redesigning the mask to minimize the length of waveguide that passes directly underneath the metal.

Because of the bandwidth limit of the detector we were unable to obtain an eye diagram for data rates greater than 20 Gbit/s at 2  $\mu$ m wavelength, but since the bandwidth of the PN junction should be very similar at both wavelengths, we expect that the modulator can operate at higher data rates at 2  $\mu$ m.

## B. Ring Resonator

### 1. Ring Resonator under Carrier Depletion

In DC measurements, the ring modulator was driven from 0 V to  $-10$  V reverse bias to produce a resonance shift of approximately 11 pm/V at 4 V bias at a wavelength of 1937 nm. The modulation efficiency is calculated using

$$V_{\pi} L_{\pi} = \frac{V \cdot \text{FSR} \cdot \pi R}{\Delta \lambda}, \quad (3)$$

where  $V$  is the applied voltage, FSR is the measured free spectral range of 16.7 nm,  $R$  is the radius of the ring modulator, and  $\Delta \lambda$  is the resonance shift. From 1–10 V reverse bias, the  $V_{\pi} \cdot L_{\pi}$  ranges from 4.4 – 6.4 V  $\cdot$  cm. The measured resonance shift is shown in Fig. 12. It agrees reasonably well with the simulation predictions. The simulated resonance shift is derived from the effective index change of the phase shifter using the equation [31]

$$\Delta \lambda_{\text{res}} = \frac{\Delta n_{\text{eff}} \cdot \lambda_{\text{res}}}{n_g}, \quad (4)$$

where  $\Delta n_{\text{eff}}$  is the change in the effective index;  $\lambda_{\text{res}}$  is the center of resonance frequency (1937 nm in this case); and  $n_g$  is the group index, which we deduced from a simulation to be 3.669.

### 2. Ring Resonator under Carrier Injection

We also performed the characterization of the same ring under forward bias. Figure 13(a) shows the normalized ring spectral

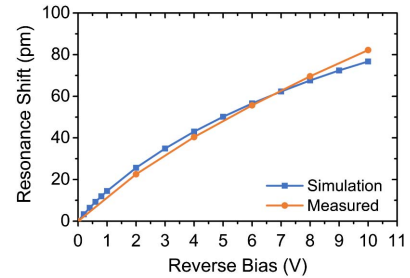


**Fig. 12.** Experiment and simulated resonance shift for a 10  $\mu$ m radius ring modulator with 64% PN junction coverage for a wavelength of 1937 nm.

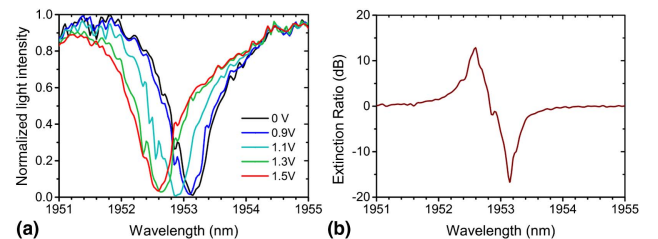


**Fig. 13.** DC characterization results for the microring modulator. (a) Ring response shift under various forward bias voltages. (b) Extinction ratio of the transmitted power between 0–1.5 V forward bias.



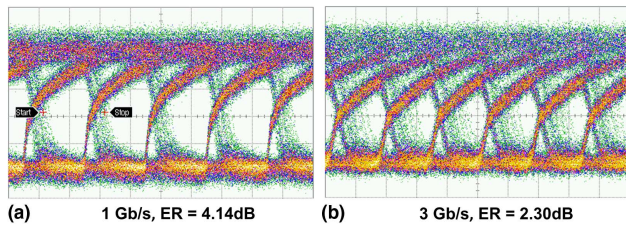


**Fig. 14.** Eye diagrams for the microring modulator at 1954 nm wavelength. (a) Data rate is 1 Gb/s, extinction ratio is 4.14 dB. (b) Data rate is 3 Gb/s, extinction ratio is 2.30 dB.

response under various forward biases, and the PN junction is not on until the forward bias is above 0.7 V. It shows an extinction ratio of 15 dB with a forward bias of 1.5 V as illustrated in Fig. 13(b).

In RF testing, to maximize the extinction ratio the device is operated in a hybrid forward and reverse bias mode. To avoid RF reflection, a low power modulator driver on the TSMC 40 nm process has been used. The optical modulator chip and electrical driver chip are connected electrically by wire bonding and are both mounted on a printed circuit board with DC power supply. The high-speed test is carried out with the driver output amplitude of 2 V. By tuning the DC reverse bias voltage, a voltage swing of  $-0.5 - 1.5$  V is applied to the device. The eye diagrams of RF testing are given in Fig. 14. The ring modulates at a data rate of 1 Gb/s with an extinction ratio of 4.14 dB. At a data rate of 3 Gb/s the extinction ratio is 2.30 dB with a power consumption of 2.38 pJ/bit.

## 5. CONCLUSION

We have filled a gap in the development of active components for a 2  $\mu\text{m}$  telecommunication system by demonstrating SOI-based high-speed modulators operating at a wavelength of 1950 nm. The effect of increased wavelength on modulator performance has been analyzed. Simulations have been performed to investigate the design trade-offs. When increasing the wavelength from 1550–1950 nm, expansion of the optical mode will cause more interaction with the highly doped regions, but the carrier effect is also stronger. With carefully selected parameters, high-speed modulation at 2  $\mu\text{m}$  is achievable and should have similar performance as in the 1550 nm regime. Experimentally, the carrier-depletion modulator has been designed for broadband operation, enabling us to compare its performance at both 1550 nm and 1950 nm. The device modulation efficiency at 4 V reverse bias is  $2.68 \text{ V} \cdot \text{cm}$  for 1950 nm and  $2.02 \text{ V} \cdot \text{cm}$  for 1550 nm. The slightly lower efficiency at 1950 nm is due to a larger optical mode that is caused by a lower overlapping factor with the depletion region in the PN junction. The device operates at a data rate of 20 Gbit/s with an extinction ratio of 5.8 dB and 30 Gbit/s with an extinction ratio of 7.1 dB for 1950 nm and 1550 nm, respectively. The wavelength should have very little effect on the bandwidth, and the difference is mainly caused by the bandwidth limit of the 2  $\mu\text{m}$  measurement setup, due mostly to the bandwidth limit of the high-speed detector. We also show a ring modulator modulating in carrier depletion mode with 43 pm resonance shift under 4 V reverse bias. Driven by a low power integrated driver the ring works in a hybrid carrier injection and depletion mode at a data rate of 3 Gbit/s with extinction ratio

of 2.30 dB and power consumption of 2.38 pJ/bit in the 2  $\mu\text{m}$  wavelength range.

All data supporting this study are openly available from the University of Southampton repository at <http://doi.org/10.5258/SOTON/D0467>.

**Funding.** Engineering and Physical Sciences Research Council (EPSRC) (EP/L01162X/1, EP/L021129/1, EP/N00762X/1); Royal Academy of Engineering (M. Nedeljkovic fellowship RF201617/16/33); National Research Foundation Singapore (NRF) (NRF-CRP12-2013-04); Royal Society (D. J. Thomson Fellowship UF150325).

## REFERENCES

1. D. J. Richardson, "Filling the light pipe," *Science* **330**, 327–328 (2010).
2. A. Ellis, D. Rafique, and S. Sygletos, "Capacity in fiber optic communications—the case for a radically new fiber," in *IEEE Photonic Society 24th Annual Meeting* (IEEE, 2011).
3. P. J. Roberts, F. Couny, H. Sabert, B. J. Mangan, D. P. Williams, L. Farr, M. W. Mason, A. Tomlinson, T. A. Birks, J. C. Knight, and P. St. J. Russell, "Ultimate low loss of hollow-core photonic crystal fibres," *Opt. Express* **13**, 236–244 (2005).
4. E. Desurvire, C. Kazmierski, F. Lelarge, X. Marcadet, A. Scavennec, F. Kish, D. Welch, R. Nagarajan, C. Joyner, R. Schneider, S. Corzine, M. Kato, P. Evans, M. Ziari, A. Dentai, J. Pleumeeckers, R. Muthiah, S. Bigo, M. Nakazawa, D. Richardson, F. Poletti, M. Petrovich, S. Alam, W. Loh, and D. Payne, "Science and technology challenges in XXIst century optical communications," *C. R. Physique* **12**, 387–416 (2011).
5. K. Nagayama, M. Kakui, M. Matsui, T. Saitoh, and Y. Chigusa, "Ultra-low-loss (0.1484 dB/km) pure silica core fibre and extension of transmission distance," *Electron. Lett.* **38**, 1168–1169 (2002).
6. C. J. Hensley, D. G. Ouzounov, A. L. Gaeta, N. Venkataraman, M. T. Gallagher, and K. W. Koch, "Silica-glass contribution to the effective non-linearity of hollow-core photonic band-gap fibers," *Opt. Express* **15**, 3507–3512 (2007).
7. F. Poletti, N. V. Wheeler, M. N. Petrovich, N. Baddela, E. N. Fokoua, J. R. Hayes, D. R. Gray, Z. Li, R. Slavik, and D. J. Richardson, "Towards high-capacity fibre-optic communications at the speed of light in vacuum," *Nat. Photonics* **7**, 279–284 (2013).
8. R. Slavik, G. Marra, E. N. Fokoua, N. Baddela, N. V. Wheeler, M. Petrovich, F. Poletti, and D. J. Richardson, "Ultralow thermal sensitivity of phase and propagation delay in hollow core optical fibres," *Sci. Rep.* **5**, 15447 (2015).
9. L. Olanterä, C. Sigaud, J. Troska, F. Vasey, M. N. Petrovich, F. Poletti, N. V. Wheeler, J. P. Wooler, and D. J. Richardson, "Gamma irradiation of minimal latency hollow-core photonic bandgap fibres," *J. Instrum.* **8**, C12010 (2013).
10. R. Soref, "Group IV photonics: enabling 2  $\mu\text{m}$  communications," *Nat. Photonics* **9**, 358–359 (2015).
11. Z. Li, A. M. Heidt, N. Simakov, Y. Jung, J. M. O. Daniel, S. U. Alam, and D. J. Richardson, "Diode-pumped wideband thulium-doped fiber amplifiers for optical communications in the 1800–2050 nm window," *Opt. Express* **21**, 26450–26455 (2013).
12. Z. Li, A. M. Heidt, J. M. O. Daniel, Y. Jung, S. U. Alam, and D. J. Richardson, "Thulium-doped fiber amplifier for optical communications at 2  $\mu\text{m}$ ," *Opt. Express* **21**, 9289–9297 (2013).
13. D. E. Hagan and A. P. Knights, "Mechanisms for optical loss in SOI waveguides for mid-infrared wavelengths around 2  $\mu\text{m}$ ," *J. Opt.* **19**, 025801 (2016).
14. Z. Liu, Y. Chen, Z. Li, B. Kelly, R. Phelan, J. O'Carroll, T. Bradley, J. P. Wooler, N. V. Wheeler, A. M. Heidt, T. Richter, C. Schubert, M. Becker, F. Poletti, M. N. Petrovich, S. U. Alam, D. J. Richardson, and R. Slavik, "High-capacity directly modulated optical transmitter for 2  $\mu\text{m}$  spectral region," *J. Lightwave Technol.* **33**, 1373–1379 (2015).
15. Y. Chen, Z. Liu, S. R. Sandoghchi, G. T. Jasion, T. D. Bradley, E. N. Fokoua, J. R. Hayes, N. V. Wheeler, D. R. Gray, B. J. Mangan, R. Slavik, F. Poletti, M. N. Petrovich, and D. J. Richardson, "Multi-kilometer long, longitudinally uniform hollow core photonic bandgap fibers for broadband low latency data transmission," *J. Lightwave Technol.* **34**, 104–113 (2016).

16. J. J. Ackert, D. J. Thomson, L. Shen, A. C. Peacock, P. E. Jessop, G. T. Reed, G. Z. Mashanovich, and A. P. Knights, "High-speed detection at two micrometres with monolithic silicon photodiodes," *Nat. Photonics* **9**, 393–396 (2015).
17. G. T. Reed, G. Z. Mashanovich, F. Y. Gardes, M. Nedeljkovic, Y. Hu, D. J. Thomson, K. Li, P. R. Wilson, S.-W. Chen, and S. S. Hsu, "Recent breakthroughs in carrier depletion based silicon optical modulators," *Nanophotonics* **3**, 229–245 (2014).
18. X. Xiao, M. Li, L. Wang, D. Chen, Q. Yang, and S. Yu, "High speed silicon photonic modulators," in *Optical Fiber Communication Conference* (OSA, 2017).
19. M. Nedeljkovic, R. Soref, and G. Z. Mashanovich, "Free-carrier electro-refraction and electroabsorption modulation predictions for silicon over the 1-14- $\mu\text{m}$  infrared wavelength range," *IEEE Photon. J.* **3**, 1171–1180 (2011).
20. M. A. V. Camp, S. Assefa, D. M. Gill, T. Barwicz, S. M. Shank, P. M. Rice, T. Topuria, and W. M. J. Green, "Demonstration of electrooptic modulation at 2165 nm using a silicon Mach-Zehnder interferometer," *Opt. Express* **20**, 28009–28016 (2012).
21. H. Zhang, N. Kavanagh, Z. Li, J. Zhao, N. Ye, Y. Chen, N. V. Wheeler, J. P. Wooler, J. R. Hayes, S. R. Sandoghchi, F. Poletti, M. N. Petrovich, S. U. Alam, R. Phelan, J. O'Carroll, B. Kelly, L. Grüner-Nielsen, D. J. Richardson, B. Corbett, and F. C. G. Gunning, "100 Gbit/s WDM transmission at 2  $\mu\text{m}$  transmission studies in both low-loss hollow core photonic bandgap fiber and solid core fiber," *Opt. Express* **23**, 4946–4951 (2015).
22. M. U. Sadiq, H. Zhang, J. O'Callaghan, B. Roycroft, N. Kavanagh, K. Thomas, A. Gocalinska, Y. Chen, T. Bradley, J. R. Hayes, Z. Li, S.-U. Alam, F. Poletti, M. N. Petrovich, D. J. Richardson, E. Pelucchi, P. O'Brien, F. H. Peters, F. Gunning, and B. Corbett, "40 Gb/s WDM transmission over 1.15-km HC-PBGF using an InP-based Mach-Zehnder modulator at 2  $\mu\text{m}$ ," *J. Lightwave Technol.* **34**, 1706–1711 (2016).
23. S. Liu, K. Xu, Q. Song, Z. Cheng, and H. Tsang, "Design of mid-infrared electro-optic modulators based on aluminum nitride waveguides," *J. Lightwave Technol.* **34**, 3837–3842 (2016).
24. N. Yahyaoui, N. Sfina, J.-L. Lazzari, A. Bournel, and M. Said, "Stark shift of the absorption spectra in Ge/Ge<sub>1-x</sub>Sn<sub>x</sub>/Ge type-i single QW cell for mid-wavelength infra-red modulators," *Superlattices Microstruct.* **85**, 629–637 (2015).
25. L. Shen, N. Healy, C. J. Mitchell, J. S. Penades, M. Nedeljkovic, G. Z. Mashanovich, and A. C. Peacock, "Mid-infrared all-optical modulation in low-loss germanium-on-silicon waveguides," *Opt. Lett.* **40**, 268–271 (2015).
26. T. Li, M. Nedeljkovic, N. Hattasan, A. Z. Khokhar, S. A. Reynolds, S. Stankovic, M. Banakar, W. Cao, Z. Qu, C. G. Littlejohns, J. S. Penades, K. Grabska, L. Mastronardi, D. J. Thomson, F. Y. Gardes, G. T. Reed, H. Wu, Z. Zhou, and G. Z. Mashanovich, "Mid-infrared Ge-on-Si electro-absorption modulator," in *IEEE 14th International Conference on Group IV Photonics (GFP)* (IEEE, 2017).
27. D. J. Thomson, L. Shen, J. J. Ackert, E. Huante-Ceron, A. P. Knights, M. Nedeljkovic, A. C. Peacock, and G. Z. Mashanovich, "Optical detection and modulation at 2  $\mu\text{m}$ –25  $\mu\text{m}$  in silicon," *Opt. Express* **22**, 10825–10830 (2014).
28. J. Kang, M. Takenaka, and S. Takagi, "Novel Ge waveguide platform on Ge-on-insulator wafer for mid-infrared photonic integrated circuits," *Opt. Express* **24**, 11855–11864 (2016).
29. R. Soref and B. Bennett, "Electrooptical effects in silicon," *IEEE J. Quantum Electron.* **23**, 123–129 (1987).
30. A. B. Fallahkhair, K. S. Li, and T. E. Murphy, "Vector finite difference modesolver for anisotropic dielectric waveguides," *J. Lightwave Technol.* **26**, 1423–1431 (2008).
31. W. Bogaerts, P. D. Heyn, T. V. Vaerenbergh, K. D. Vos, S. K. Selvaraja, T. Claes, P. Dumon, P. Bienstman, D. V. Thourhout, and R. Baets, "Silicon microring resonators," *Laser Photon. Rev.* **6**, 47–73 (2012).